 CMES, vol.49, no.3, pp.217-253, 2009

Vortex Ring Formation within a Spherical Container with Natural Convection

Gerardo Anguiano-Orozco[1,2] **and Rubén Avila** [3]

Abstract: A numerical investigation of the transient, three dimensional, laminar natural convection of a fluid confined in a spherical container is carried out. Initially the fluid is quiescent with a uniform temperature T_i equal to the temperature of the wall of the container. At time t=0, the temperature of the wall is suddenly lowered to a uniform temperature T_w=0. The natural convection, that conducts to a vortex ring formation within the sphere, is driven by a terrestrial gravity force (laboratory gravity) and by the step change in the temperature of the wall. A scaling analysis of a simplified transient, two dimensional model, formulated in the cylindrical coordinate system, provides a qualitative description of the flow in the spherical enclosure, from start up (including the three stages of the transient process: boundary layer development, stratification and cooling-down) to the time at which the system reaches the new thermal equilibrium condition (uniform temperature T_w) without motion. The governing three dimensional Navier-Stokes equations for an incompressible fluid, formulated in the Cartesian coordinate system, have been numerically solved by using the h/p spectral element method. The Rayleigh number is in the range: $1 \times 10^3 \leq Ra \leq 1.5 \times 10^5$. The average Nusselt number $\overline{Nu}$ as a function of time is evaluated at the wall of the container. The results provided by the spectral element method are in agreement with the scaling analysis results for low Ra numbers, $Ra \leq 1 \times 10^4$. As the Ra number is increased, in the range: $1 \times 10^5 \leq Ra \leq 1.5 \times 10^5$, the flow becomes unstable and oscillatory in the stratification stage. The temperature, vorticity and pressure fields for the three stages of the transient process are presented.

Keywords: Vortex ring, non-steady natural convection, scaling laws.

[1] Facultad de Ciencias, UAEM, Av. Instituto Literario 100, C.P. 50000 Toluca, México.

[2] Depto. de Física, Instituto Nacional de Investigaciones Nucleares, Apdo. Postal 18-1027, gerardo.anguiano@gmail.com.

[3] Departamento de Termofluidos, Facultad de Ingeniería, Universidad Nacional Autónoma de México, Mexico D.F., C.P. 04510, ravila@servidor.unam.mx.

1 Introduction

Non-steady and three dimensional heat transfer analysis of a fluid confined in closed containers, has been the subject of a great number of investigations. The research work aimed to: (i) quantify the heat transfer from the wall of the container to the fluid (or the reverse), (ii) predict the flow patterns to obtain an optimal heat transfer rate, or (iii) estimate the map of instabilities of the system, to obtain the relevant parameters that lead to transition of the flow; have been carried out by experimental techniques, numerical solutions, instability analysis techniques or by scaling analysis methods. However the study of the three dimensional, transient natural convection of a fluid confined in spherical enclosures, has been limited, even though this system appears frequently in industrial applications and natural phenomena. In industry the motion by natural convection of a great mass of natural gas or fuel liquids within spherical reservoirs, is an important mechanical design parameter, particularly if the container is located in regions where the ambient temperature may change suddenly. In nature, the natural convection of fluids within spherical enclosures is found in drops, and in the core of stars and planets.

In the literature there are few papers dealing with the subject of non-steady natural convection in spherical enclosures [Whitley-III and Vachon (1972); Chow and Akins (1975); Hutchins and Marschall (1989); Zhang, Khodadadi, and Shen (1999)]. However it is not possible to find a full three dimensional, unsteady numerical analysis of the flow, particularly at high Rayleigh numbers Ra, where the flow becomes oscillatory with erratic motion [Chow and Akins (1975)]. Whitley-III and Vachon (1972) carried out a numerical solution of the Navier-Stokes equations formulated in terms of stream function and vorticity. Their simplified two dimensional axisymmetric model was solved by using the finite difference numerical method. In their physical model it was assumed that the temperature at the wall of the sphere was suddenly increased. Their main findings are the following: (i) higher velocities are located near the wall, (ii) a semi-circular flow pattern is obtained where the upward heated flow forces the cooler fluid to the lower region of the sphere, (iii) heat transfer by convection dominates that by conduction, and (iv) in the region surrounding the bottom, oscillations occur in the temperature field. Chow and Akins (1975) carried out an experimental investigation of the pseudosteady-sate natural convection of water contained within spherical containers of different sizes. The pseudosteady-state condition was reproduced by continuously increasing the temperature of the external bath surrounding the sphere such that the temperature difference between the bath and the center of the sphere had a constant value. Flow patterns, the effect of the Rayleigh number Ra on the location of the circulation center of the vortex in the sphere, and the heat transfer rate correlation (average Nusselt number $\overline{Nu}$ as a function of the Ra number) were reported for the case of

a sudden increase of the temperature at the wall of the sphere. The main findings of their research are the following: (i) laminar flow prevails below *Ra* numbers of about 1×10^7, (ii) at small times after the beginning of the heating the fluid near the wall moved up along the wall and down in the large central core, (iii) as the *Ra* number is increased between 1×10^5 and 1×10^7, the circulation center is displaced towards the wall and downward from the horizontal line (along the equator), and (iv) turbulent flow (or perhaps transitional flow) was found for *Ra* numbers greater than 10^7. At these high *Ra* numbers they found that the circulation center was initially above the horizontal axis but moved down after a short time, but after a certain time the fluid at the bottom moved vertically in a swirl and spread out somewhere near the center, leading to an erratic fluid motion with an irregular flow pattern. Hutchins and Marschall (1989), carried out a numerical investigation of the pseudosteady-state natural convection of the fluid inside a closed spherical container. They solved the two dimensional governing equations (formulated in spherical coordinates and in terms of the stream function and vorticity) by a finite difference method. The range of the *Ra* number that they used in their calculations was $1 \times 10^5 < Ra < 1 \times 10^8$ and the Prandtl number *Pr* was in the range $0.7 < Pr < 8$. A heating condition (at t=0 a step increase of the temperature at the wall was assumed) of the fluid from the wall was studied. Their main findings are the following: (i) the circulation moves towards the wall for increasing *Ra* number, and (ii) high temperature gradients appear close to the wall in the lower hemisphere, The main drawback of the work carried out by Hutchins and Marschall (1989) is that their model was two-dimensional and it was not able to reproduce the experimental data produced by Chow and Akins (1975), in the sense that for $Ra > 1 \times 10^7$, the flow is oscillatory. Zhang, Khodadadi, and Shen (1999) carried out a numerical study of the pseudosteady-state natural convection within spherical containers partially filled with a porous medium. The analysis was very similar to the investigation previously performed by Hutchins and Marschall (1989). The governing two dimensional equations formulated in the spherical coordinate system and in primitive variables were solved by using the finite-volume method. In the first part of their paper (system without porous medium), Zhang, Khodadadi, and Shen (1999), attempted to reproduce the experimental findings previously published by Chow and Akins (1975). Their main findings corresponding to the part without porous medium are the following: (i) at the early stages the dominant heat transfer mechanism is by conduction, then the flow pattern leads to a temperature field in which the isotherm lines are concentric circles independent of the polar angle, (ii) as time elapses, natural convection is dominant and the isotherm lines become skewed, as the *Ra* number is increased the degree of skew is higher, and (iii) the center of the circulation pattern is dependent on the *Ra* number and moves towards the wall as *Ra* increases. The lack of a three dimensional simulation did

not allow to Zhang, Khodadadi, and Shen (1999) to reproduce the experimental findings previously reported by Chow and Akins (1975), particularly for the cases with $Ra > 1 \times 10^7$, in which the flow is oscillatory.

In this paper we present a numerical solution of the natural convection of a fluid that is confined in a spherical enclosure. The non-steady, three dimensional, Boussinesq governing equations are solved by using the h/p spectral element method. The Ra numbers taken into account in this study are in the range $1 \times 10^3 \leq Ra \leq 1.5 \times 10^5$. For the low Ra number regime, $Ra \leq 1 \times 10^4$, the flow pattern is two dimensional and does not present oscillations. However as the Ra number is increased an oscillatory behaviour of the flow is observed. For low Ra numbers, the heat transfer rate at the wall of the sphere (the average Nusselt number $\overline{Nu}$) is a monotonic decreasing function of time, but at high Ra number, due to the oscillations of the flow field, the average $\overline{Nu}$ number, also shows an oscillatory behaviour. In order to understand the whole cooling down process, the transient evolution of the system is analyzed by performing a scale analysis, which is based in a simplified transient, two dimensional model that is formulated in the cylindrical coordinate system. The whole cooling down process has been divided into three stages (i) the boundary layer development stage, (ii) the stratification stage, and (iii) the cooling down stage. The vortex ring formation theory, that takes into account the vorticity field and the circulation in the flow domain, has been used to estimate the characteristic time scales and the amount of entrainment, from the flow adjacent to the wall towards the core of the sphere. In section 2 the description of the physical model under study is presented. In section 3 we present the governing equations. In section 4 we present an overview of the spectral element method that we used to solve the governing equations. Section 5 shows the process that we follow to develop the scaling laws, together with the obtained numerical results for the three stages. A comparison between the numerical solution and the scaling laws results is also presented in section 5. In section 6 we present a discussion on the general characteristics of a three dimensional unstable oscillating vortex ring. Finally in section 7 the concluding remarks are presented.

2 Physical Model

The physical system under study is an initially quiescent incompressible fluid that is confined in a spherical container. The fluid and the wall of the container are initially at the same uniform temperature T_i. At time t=0, the temperature of the wall is suddenly changed to a uniform temperature T_w. In all the cases analyzed in this paper we have assumed that $T_i > T_w$. The gravity force acting on the fluid has a constant value and it is oriented along the x_3 direction of a Cartesian coordinate system (see Fig. 1). The temperature gradients that appear in the interior of the fluid due to

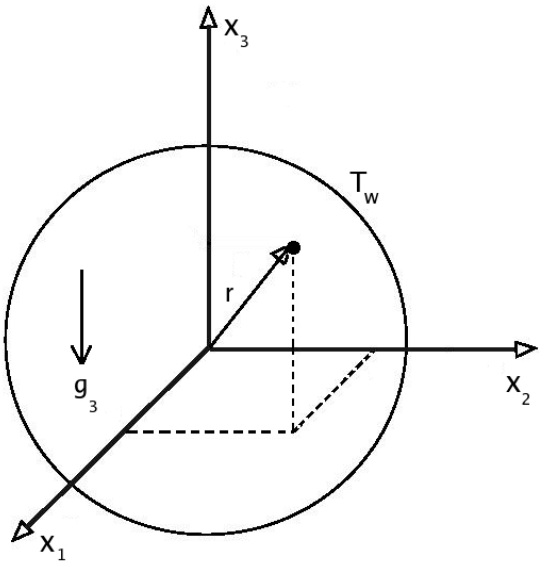

Figure 1: Physical model of the non-steady natural convection in spherical containers. The origin of the Cartesian coordinate system is located at the centre of the sphere.

the step change in the temperature of the wall, lead to a time dependent magnitude of the buoyancy force which promotes the presence of natural convection motion. The induced convective flow patterns are responsible for the heat transfer process from the fluid towards the wall. The time that must be elapsed prior the system attains a new equilibrium condition at some subsequent time, strongly depends on the flow patterns of the fluid which appear during the transient process from t=0 to the new equilibrium state.

3 Mathematical model

We assume that the spherical enclosure contains a Newtonian, viscous, incompressible fluid. The physical properties of the fluid remain constant with the exception of the density whose variation with temperature (linearized over the range of interest, Boussinesq approximation) is taken into account in the buoyancy term of the momentum equation. In the model it is also assumed that the thermal energy dissipation rate by viscous heating is neglected. By using the following dimensionless variables (denoted by the use of the superscript $*$):

$$x_j^* = \frac{x_j}{R}, \quad v_j^* = \frac{Rv_j}{\alpha}, \quad t^* = \frac{\alpha t}{R^2}, \quad T^* = \frac{T-\overline{T}}{\overline{T}_i - T_w}, \quad p^* = \frac{R^2 p}{\rho_o \alpha^2}, \quad r^* = \frac{r}{R}, \quad (1)$$

where x_j are the Cartesian coordinates (using indicial notation), v_j are the velocities of the fluid, R is the radius of the sphere, $r = \left(x_1^2 + x_2^2 + x_3^2\right)^{1/2}$ is the radial coordinate of a point in the sphere, α is the thermal diffusivity, t is the time, p is the pressure, ρ_o is the reference fluid density, T_w is the temperature of the wall, $\overline{T}_i$ is the initial average temperature of the fluid and $\overline{T}$ is the average temperature of the fluid as a function of time, the dimensionless governing equations are written as follows (leaving out the superscript $*$):

Continuity equation:

$$\nabla \cdot \mathbf{v} = 0 \quad (2)$$

Momentum equation:

$$\frac{D\mathbf{v}}{Dt} = -\nabla p + Pr\nabla^2 \mathbf{v} + RaPrT\mathbf{i}_3 \quad (3)$$

Energy equation:

$$\frac{DT}{Dt} = \nabla^2 T \quad (4)$$

where Ra is the Rayleigh number at the start up of the transient process which is defined as

$$Ra = \frac{\beta g_3 \Delta T R^3}{\nu \alpha}, \quad (5)$$

Pr is the Prandtl number $Pr = \nu/\alpha$, the dimensional $\Delta T = \overline{T}_i - T_w$, g_3 is the terrestrial gravity acceleration (laboratory gravity along the unit base vector $\mathbf{i}_3$) and β is the thermal expansion coefficient. Initially the fluid and the wall of the container are at the same uniform dimensional temperature $T_i = \overline{T}_i$, at a certain instant, the dimensional temperature of the wall is suddenly reduced to a uniform dimensional temperature T_w. Referring to the dimensionless temperature T, see Eq. (1), at t=0, the temperature within the sphere is $T(\mathbf{x}, t=0) = 0$, whereas the temperature at the wall is $T(\mathbf{x}_w, t=0) = -1$. As time elapses, the dimensionless temperature of the points within the sphere acquires positive values at the points with higher temperature than the dimensionless instantaneous average value $< T > (t)$, and negative values at the points with lower temperature than the instantaneous average value

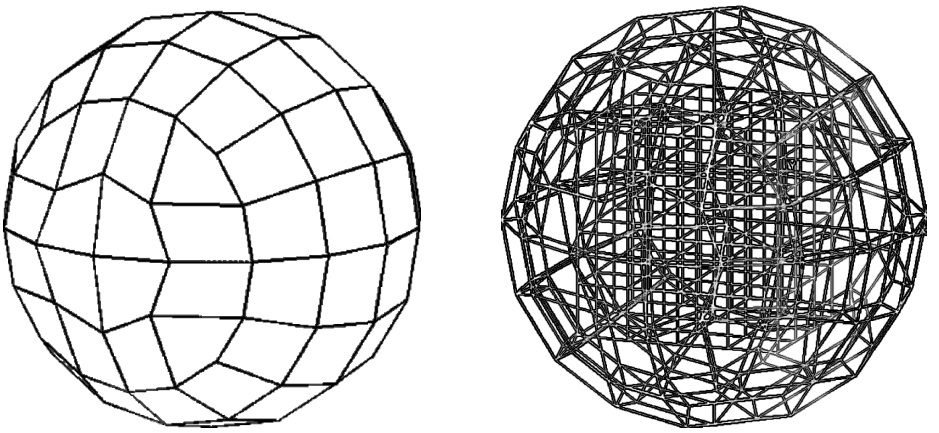

Figure 2: Spectral element method mesh with 256 non-regular hexahedra macro-elements with polynomial expansion of order 5. The algorithm used in the generation of the mesh, includes a central regular hexahedron. The origin of the Cartesian coordinate system is located at the centre of the sphere, see Fig. 1.

$< T > (t)$. As time $t \to \infty$ the points in the container tend to acquire the temperature of the wall, hence the instantaneous average temperature $< T > (t)$ also tends to the temperature of the wall, consequently the dimensionless temperature in the whole domain (including the points at the wall) tends to zero, see Eq. (1). At the solid wall, $r = R$, it is assumed a no slip boundary condition, hence $\mathbf{v} = 0$. In this investigation the Prandtl number was fixed to one, whereas the Ra number, at the beginning of the transient process, was varied in the range $1 \times 10^3 < Ra < 1.5 \times 10^5$. The dimensional values of the radius of the sphere R, temperature of the wall T_w and thermo-physical properties were selected as follows: $R = 1$ m, $T_w = 0^o$C, $\rho_o = 1$ kg/m^3, $\alpha = 1$ m^2/s, $\beta g_3 = -0.01$ m/K s^2, specific heat capacity C_p=1 J/kg K, thermal conductivity $k = 1$ W/m K and kinematic viscosity $\nu = 1$ m^2/s.

4 Numerical method

The set of Eqs. (2)-(4) has been solved by using the h/p spectral element method [Patera (1984); Rønquist (1988); Karniadakis and Sherwin (1999)]. This methodology is a special case of the method of weighted residuals which leads to the Bubnov-Galerkin formulation (the expansion functions used to approximate the dependent variables, are the same as the weight functions). Using the spectral element method, the computational domain is subdivided into large non-overlapping,

non-regular hexahedra (structured mesh), isoparametric macro-elemental regions (h-element size). Inside them, high order piecewise polynomial expansions (p-polynomial order) are defined. The spectral element method uses a polynomial nodal expansion based on Lagrange polynomials, which are associated with a set of nodal points that are located at the zeros of the Gauss-Lobatto-Legendre polynomials. The numerical quadrature is performed using a Gauss-Lobatto-Legendre quadrature rule, which corresponds to the same choice of the nodal points. Details of the numerical algorithm for the solution of the fluid equations are reported by Rønquist(1988), and Karniadakis and Sherwin(1999). The spectral element method has been successfully used to solve fluid dynamics problems as well as problems in different fields of science and technology [Avila and Solorio (2009); Mitra and Gopalakrishnan (2006); Wu, Liu, Scarpas, and Ge (2006); Wu, Al-Khoury, Kasbergen, Liu, and Scarpas (2007)]. In order to increase the performance of the spectral element method, very recently it has been successfully combined with numerical algorithms such as the fictitious domain approach and the Least-Squares method [Parussini (2007); Parussini and Pediroda (2007)]. After performing several tests to reach mesh independent results, we decided to discretize the three dimensional computational domain by using 256 non-regular hexahedra spectral elements with a piecewise polynomial expansion of order 5. Fig. 2 shows the numerical mesh. Notice that by using non-regular hexahedra with straight sides to generate the geometry of the container, it is not possible to obtain a perfect spherical shape. In order to approximate more accurately the spherical geometry we discretized the computational domain by using grids with 500 and 720 elements, with polynomial expansions of order 5. However as the number of elements is increased, the computer time required to solve the governing equations is considerably higher, on the other hand the results obtained with the 256 elements grid, were very similar to those results obtained with the 720 elements grid. The accuracy of the solution was not substantially increased probably because the numerical algorithm used to generate the grid requires, as a restriction, to have an hexahedron located at the centre of the sphere. From the central hexahedron the algorithm distributes the macro-elements within the sphere. In this research we use a container with dimensional radius $R = 1$ m, then the volume of the sphere is $V = 4.188$ m^3. The mean radius $\overline{R}$ and volume $\hat{V}$ of the quasi-sphere shown in Fig. 2 (calculated by taking into account the Gauss-Lobatto-Legendre points located at the surface) are: $\overline{R} = 0.985$ m, and $\hat{V} = 4.1284$ m^3, respectively. A remark can be given at this point. The authors want to mention that one of the advantages of using the Navier-Stokes equations formulated in the Cartesian coordinate system for the solution of problems with spherical geometry, is that we are able to avoid the singularity that appears at the poles of the sphere ("pole singularity"). It is well known that this singularity appears when the governing equations are formulated in the spherical coordinate

system. On the other hand, the drawback of using a mesh based numerical method (for the solution of the equations formulated in the Cartesian coordinate system) is that we have to discretize the domain by using non-regular hexahedra, which leads to a non-exact representation of the spherical domain. This can produce errors in the numerical solution of the fluid variables. Such limitation can be overcome by using numerical techniques which are under development in the area of fluid dynamics. These numerical algorithms are based on a meshfree approach, an example of this methodology is the Meshless Local Petrov-Galerkin (MLPG) method [Lin and Atluri (2000); Lin and Atluri (2001); Atluri, Han, and Rajendran (2004); Avila and Pérez (2008)]. Using meshfree numerical algorithms, the solution of spherical problems formulated in the Cartesian coordinate system may be reduced to the proper location of MLPG particles (or nodes) within and at the wall of the spherical cavity. Using the MLPG method we would be able to overcome simultaneously the two difficulties: (i) the singularities at the poles and (ii) the accurate representation of the spherical container.

5 Scaling analysis

In this section, scaling laws will be developed for the relevant parameters characterizing the non-steady flow behaviour within the sphere. Scaling analysis has been used as an effective and easy-to-use tool to understand the transient process of cooling an initially homogeneous fluid by natural convection in vertical circular cylinders and in rectangular cavities [Patterson and Imberger (1980); Armfield, Patterson, and Lin (2007); Lin and Armfield (2005)]. In this investigation we apply the scaling analysis for two reasons: (i) to obtain scaling laws for the basic flow features (such as velocity, thermal boundary layer thickness, and heat transfer rate) that appear when an initially quiescent fluid at a uniform dimensional temperature T_i is cooled by imposing a lower dimensional temperature T_w $(T_i > T_w)$ on the wall of the spherical container, and (ii) to obtain the formation time of the vortex ring within the sphere and to estimate the rate of the entrainment of the cold flow adjacent to the wall, into the core of the vortex ring. Similarly to the scaling analysis carried out by Lin and Armfield (2005), we assume that the flow within the sphere is dominated by three different stages of development: (i) the boundary layer stage, (ii) the stratification stage, and (iii) the cooling-down stage. In the scaling analysis, we have assumed that the flow is laminar and axisymmetric, hence the analysis is performed in the plane r-θ of the cylindrical coordinate system. The axisymmetric assumption was considered because in the numerical simulations for the cases with initial Rayleigh number $Ra < 1 \times 10^4$, the flow behaves as two-dimensional, hence the scaling analysis in the plane r-θ is fully justified. However for the cases with initial Rayleigh number $Ra = 1 \times 10^5$ and $Ra = 1.5 \times 10^5$, the non-steady flow in

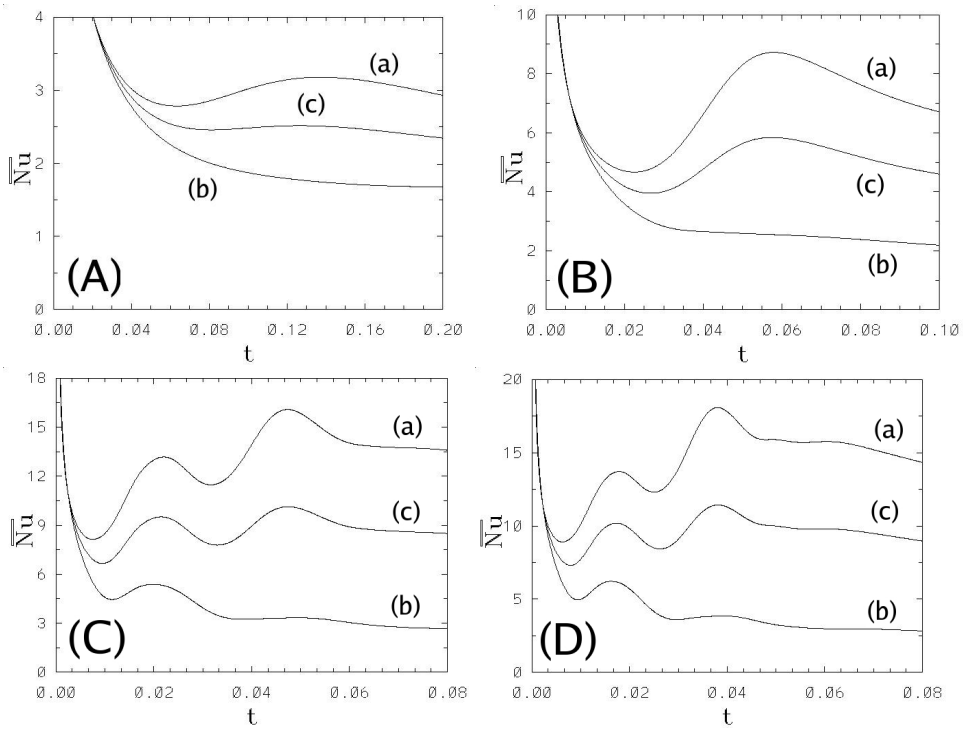

Figure 3: Average Nusselt number $\overline{Nu}$ as a function of time. Initial Rayleigh number Ra: (A) $Ra = 1 \times 10^3$, (B) $Ra = 1 \times 10^4$, (C) $Ra = 1 \times 10^5$, (D) $Ra = 1.5 \times 10^5$. (a) $\overline{Nu}$ of the upper hemisphere, (b) $\overline{Nu}$ of the lower hemisphere. and (c) $\overline{Nu}$ of the whole sphere.

the boundary layer and cooling-down stages behaves as two dimensional. But in the stratification stage we have observed an oscillatory, unstable behaviour of the flow field. Hence the scaling analysis is not valid in the stratification stage for these particular cases ($Ra = 1 \times 10^5$ and $Ra = 1.5 \times 10^5$).

For the scaling analysis, the governing equations are the Navier-Stokes equations formulated in the cylindrical coordinate system. Scaling laws will be obtained for the dimensional parameters: (i) angular velocity u_θ, (ii) the thermal boundary layer thickness δ_T, and (iii) the start up time t. Additionally the scaling law for the local Nusselt number Nu will be developed. The variables defined in Eq. (1) are used to obtain the dimensionless values of u_θ, δ_T and the start up time t.

The dimensional governing equations are the following:

Continuity equation

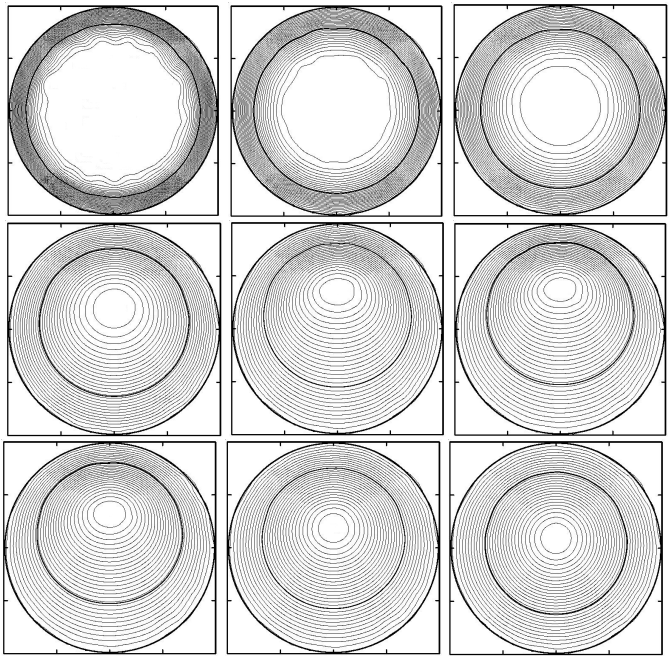

Figure 4: Numerical simulation of the dimensionless temperature contours. The boundary layer development stage: Top row, from left to right: $t = 0.01$, (-0.63,0.36); $t = 0.02$, (-0.57,0.42) and $t = 0.03$, (-0.52,0.47). The stratification stage: Middle row, from left to right: $t = 0.06$, (-0.39,0.51); $t = 0.1$, (-0.25,0.41) and $t = 0.14$, (-0.15,0.27). The cooling-down stage: Bottom row, from left to right: $t = 0.2$, (-0.08,0.14); $t = 0.3$, (-0.02,0.04) and $t = 0.4$, (-0.01,0.016). For initial Rayleigh number $Ra = 1 \times 10^3$.

$$\frac{1}{r}\frac{\partial}{\partial r}(ru_r) + \frac{1}{r}\frac{\partial u_\theta}{\partial \theta} + \frac{\partial u_z}{\partial z} = 0 \tag{6}$$

Momentum equation (angular direction)

$$\frac{\partial u_\theta}{\partial t} + u_r\frac{\partial u_\theta}{\partial r} + \frac{u_\theta}{r}\frac{\partial u_\theta}{\partial \theta} - \frac{u_r u_\theta}{r} = -\frac{1}{\rho}\frac{1}{r}\frac{\partial p}{\partial \theta} + \nu\left(\frac{1}{r}\frac{\partial}{\partial r}\left(r\frac{\partial u_\theta}{\partial r}\right) + \frac{1}{r^2}\frac{\partial^2 u_\theta}{\partial \theta^2} + \frac{2}{r^2}\frac{\partial u_r}{\partial \theta} - \frac{u_\theta}{r^2}\right) + g_\theta \tag{7}$$

Energy equation

$$\frac{\partial T}{\partial t}+u_r\frac{\partial T}{\partial r}+\frac{u_\theta}{r}\frac{\partial T}{\partial \theta}=\frac{\alpha}{r}\frac{\partial}{\partial r}\left(r\frac{\partial T}{\partial r}\right)+\frac{\alpha}{r^2}\frac{\partial^2 T}{\partial \theta^2} \tag{8}$$

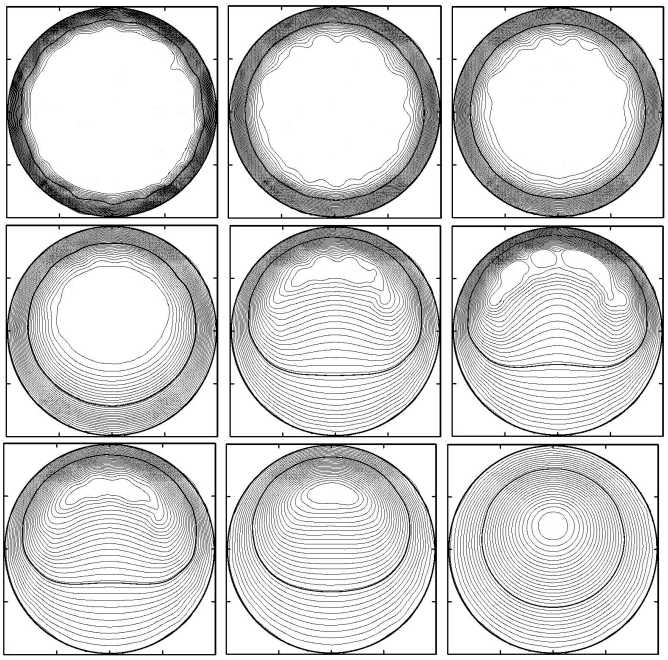

Figure 5: Numerical simulation of the dimensionless temperature contours. The boundary layer development stage: Top row, from left to right: $t = 0.004$, (-0.72,0.28); $t = 0.008$, (-0.65,0.34) and $t = 0.01$, (-0.63,0.36). The stratification stage: Middle row, from left to right: $t = 0.02$, (-0.57,0.42); $t = 0.04$, (-0.38,0.57) and $t = 0.06$, (-0.25,0.37). The cooling-down stage: Bottom row, from left to right: $t = 0.1$, (-0.13,0.22); $t = 0.2$, (-0.03,0.06) and $t = 0.4$, (-0.003,0.006). For initial Rayleigh number $Ra = 1 \times 10^4$.

5.1 Boundary layer development stage

At small times heat will be conducted out of the fluid creating a descending spherical boundary layer of thickness $O(\delta t)$ which is governed by Eq. (8). Additionally at small times, the velocity field is not fully developed hence the convective terms of Eq. (8) are small, therefore there is a balance between the temporal term and the

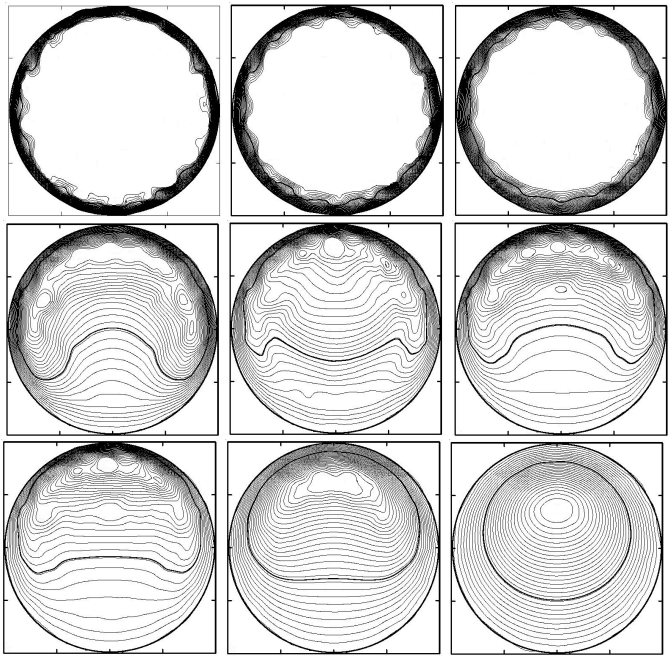

Figure 6: Numerical simulation of the dimensionless temperature contours. The boundary layer development stage: Top row, from left to right: $t = 0.001$, (-0.83,0.16); $t = 0.002$, (-0.78,0.21) and $t = 0.003$, (-0.74,0.25). The stratification stage: Middle row, from left to right: $t = 0.017$, (-0.46,0.63); $t = 0.025$, (-0.45,0.75) and $t = 0.038$, (-0.25,0.67). The cooling-down stage: Bottom row, from left to right: $t = 0.06$, (-0.14,0.43); $t = 0.2$, (-0.007,0.015) and $t = 0.4$, (-0.0006,0.001). For initial Rayleigh number $Ra = 1.5 \times 10^5$.

conductive term along the radial direction, then we have:

$$\delta_T = (\alpha t)^{1/2} \tag{9}$$

During the start up stage, the buoyancy forces accelerate the fluid, then it may be assumed that the dominant balance at a certain position $R\theta$ from the upper pole of the sphere (and for $Pr \geq 1$), is that between the buoyancy and viscous forces. Then from the momentum equation along the angular direction θ (see Eq. (7)), we can obtain a relationship for the boundary layer angular velocity during the start up stage as

$$u_\theta \sim \frac{\beta g_\theta \left(\overline{T}_i - T_w\right)}{\nu} \delta_T^2 \tag{10}$$

Using Eq. (9) into Eq. (10) we have

$$u_\theta \sim \frac{\beta g_3 \sin\theta \left(\overline{T}_i - T_w\right)}{Pr} t \tag{11}$$

where $g_\theta = g_3 \sin\theta$, is the gravity force component acting along the θ direction (as a function of the θ angle from the upper pole). As time elapses the boundary layer will continue to grow until the heat conducted out through the wall is balanced by that convected by the fluid motion towards the wall of the sphere. Balancing these terms in the energy equation will yield a scaling for the time to reach the conduction-convection balance:

$$\frac{u_\theta}{r}\frac{\partial T}{\partial \theta} \sim \frac{\alpha}{r}\frac{\partial}{\partial r}\left(r\frac{\partial T}{\partial r}\right) \tag{12}$$

by substituting Eq. (11) into Eq. (12) we obtain

$$t_b \sim \left(\frac{\nu R\theta}{\alpha\beta g_3 \sin\theta \left(\overline{T}_i - T_w\right)}\right)^{1/2} \sim \frac{(R\theta)^2}{\alpha}\frac{1}{Ra_\theta^{1/2}} \tag{13}$$

where Ra_θ is the Rayleigh number based on the position $R\theta$ from the upper pole, $Ra_\theta = \beta g_3 \sin\theta \left(\overline{T}_i - T_w\right)(R\theta)^3/\nu\alpha$. Eq. (13) provides the time t_b at which the conduction-convection balance is attained (for a certain angular position at the wall $R\theta$, and for a given initial Rayleigh number Ra_θ). Once t_b is calculated, it is possible to evaluate the boundary layer thickness $\delta_{T,b}$ as (see Eq. (9)):

$$\delta_{T,b} \sim \frac{R\theta}{Ra_\theta^{1/4}} \tag{14}$$

and the angular velocity $u_{\theta,b}$ as (see Eq. (11)):

$$u_{\theta,b} \sim \frac{\alpha}{(R\theta)} Ra_\theta^{1/2} \tag{15}$$

The heat transfer (at the position $R\theta$) across the spherical wall is represented by the local Nusselt number Nu, which is defined as

$$Nu = \frac{hR}{k}, \tag{16}$$

where the local convective heat transfer coefficient h is defined as

$$h = \left(\frac{k}{\overline{T}_i - T_w} \frac{\partial T}{\partial r} \right)_{r=R}. \tag{17}$$

Therefore, during the start up stage, the local Nusselt number can be written as

$$Nu \sim \frac{R}{\delta_T} \sim \frac{R}{(\alpha t)^{1/2}}, \tag{18}$$

hence in the conduction-convection balance stage we have

$$Nu_b \sim \frac{R}{\delta_{T,b}} \tag{19}$$

The results obtained by the numerical simulation (carried out in a Cartesian coordinate system) and by the scaling analysis (performed in a cylindrical coordinate system), for different initial Ra numbers in the range $1 \times 10^3 \leq Ra \leq 1.5 \times 10^5$, in which we have observed in the boundary layer development stage a two dimensional behaviour, will be presented. The results of the scaling analysis for four different initial Ra numbers are shown in Tab. 1. The dimensionless parameters t_b, $\delta_{T,b}$, $u_{\theta,b}$, and Nu_b (evaluated at $\theta = \pi/2$), have been obtained by using Eqs. (13), (14), (15) and (19) respectively and the variables defined in Eq. (1).

Table 1: Dimensionless scaling analysis results (at $\theta = \pi/2$) for the boundary layer development stage. t_b see Eq. (13), $\delta_{T,b}$ see Eq. (14), $u_{\theta,b}$ see Eq. (15), Nu_b see Eq. (19), t_o see Eq. (22) and $u/2$ see Eq. (24).

Ra	Ra_θ	t_b	t_o	$\delta_{T,b}$	$u_{\theta,b}$	$u/2$	Nu_b
10^3	3875.7	0.039	0.031	0.19	39.6	31.6	5
10^4	38757.8	0.012	0.01	0.11	125.3	100	9
10^5	387578.4	0.0039	0.0031	0.062	396.3	316.2	16
1.5E10^5	581367.6	0.0032	0.0025	0.056	485.4	387.2	17.8

Fig. 3 shows the average Nusselt number $\overline{Nu}$, evaluated at the wall of the container, as a function of time. We present for each case under study (see Tab. 1) three curves. The upper curve (a) is the $\overline{Nu}_n$ evaluated on the north (upper) hemisphere. The lower curve (b) represents the $\overline{Nu}_s$ evaluated on the south (lower) hemisphere. And the middle curve (c) corresponds to the $\overline{Nu}_w$ evaluated on the whole spherical wall. For the case with initial Rayleigh number 1×10^3 (see Fig. 3A), the

three curves overlap for dimensionless time $t \leq 0.03$. The explanation of this behaviour is that at $t \leq 0.03$, the flow patterns in both hemispheres is the same. This condition can only be valid when the diffusion terms are dominant and the flow remains adjacent to the wall (there is no entrainment of the cold fluid adjacent to the wall towards the hot fluid in the core, see Sec. 5.2), hence at small times we have the boundary layer development stage. It is observed that at $t_b \approx 0.03$, the $\overline{Nu}_n \approx \overline{Nu}_s \approx \overline{Nu}_w = \overline{Nu} \approx 3.3$, which is in qualitative agreement with the scaling analysis results (see Tab. 1). It has to be mentioned that in the scaling analysis we have calculated the local Nu at the angular position $\theta = \pi/2$, which is the maximum local Nu number at the spherical wall, whereas in Fig. 3 we report the average Nusselt number $\overline{Nu}$. In terms of scaling analysis we may conclude that this is qualitatively valid, because we only want to consider the order of approximation between the scaling laws and the numerical simulations. Fig. 3A also shows that for times $t \geq 0.03$, begins the separation between the $\overline{Nu}_n$ and $\overline{Nu}_s$ curves. It is seen that for times $t \geq 0.03$, the negative slope of the $\overline{Nu}_n$ curve is reduced, and at a certain time $t \geq 0.07$ the slope becomes positive, afterwards the $\overline{Nu}_n$ curve attains a maximum value at $t \approx 0.14$. On the other hand, it is clearly observed that the $\overline{Nu}_s$ curve always decreases, this behaviour of the heat transfer at the wall, is the effect of two phenomena occurring in the south hemisphere: (i) the velocity of the flow is reduced and (ii) the mass of fluid is reduced due to the stratification of the cavity (by the entrained cold fluid adjacent to the wall in the region surrounding the equator). Therefore we may conclude that in the time interval $0.03 \leq t \leq 0.14$, we have the stratification stage (which will be explained in Sec. 5.2). Fig. 3A shows that for times $t \geq 0.14$, the Nusselt numbers $\overline{Nu}_n$ and $\overline{Nu}_w$ continuously decrease, which means that the dimensional average instantaneous temperature $\overline{T}(t)$ is diminishing (tending to the dimensional value of the wall T_w) and the buoyancy force is continuously reduced (cooling-down stage, see Sec. 5.3). A similar description can be given for the other cases shown in Fig. 3. When $Ra = 1 \times 10^4$ (see Fig. 3B), the boundary layer development stage ends at $t_b \approx 0.01$, with an average Nusselt number $\overline{Nu} \approx 6.4$, which is in qualitative agreement with the scaling analysis results (see Tab. 1). The stratification stage is in the interval $0.01 \leq t \leq 0.06$, and the cooling-down stage begins at $t \approx 0.06$. When $Ra = 1 \times 10^5$ (see Fig. 3C), the boundary layer development stage ends at $t_b \approx 0.004$, with an average Nusselt number $\overline{Nu} \approx 9.2$, which is in qualitative agreement with the scaling analysis results (see Tab. 1). The stratification stage is in the interval $0.004 \leq t \leq 0.046$ (with an oscillatory behaviour), and the cooling-down stage begins at $t \approx 0.046$. Similarly when $Ra = 1.5 \times 10^5$ (see Fig. 3D), the boundary layer development stage ends at $t_b \approx 0.003$, with an average Nusselt number $\overline{Nu} \approx 10.5$, which is in qualitative agreement with the scaling analysis results (see Tab. 1). The stratification stage is in the interval $0.003 \leq t \leq 0.036$ (with an oscillatory behaviour), and the

cooling-down stage begins at $t \approx 0.036$.

Fig. 4 shows the dimensionless isotherm lines (see Eq. (1)) for the three stages when the initial Rayleigh number is $Ra = 1 \times 10^3$. Panels on the top row show the boundary layer development stage (at $t = 0.01$, $t = 0.02$ and $t = 0.03$). Panels on the middle row show the stratification stage (at $t = 0.06$, $t = 0.1$ and $t = 0.14$). And panels on the bottom row show the cooling-down stage (at $t = 0.2$, $t = 0.3$ and $t = 0.4$). The meridional plane shown in Fig. 4 (and in the whole set of figures presented in this paper) corresponds to the plane whose normal unit vector is $\mathbf{i}_1$ (the first base unit vector of the Cartesian coordinate system). In each of the figures, we have plotted twenty nine dimensionless isotherm lines equally spaced between the minimum and the maximum values of the temperature field. These values are written within the round brackets in the caption of each figure. An additional isotherm line is plotted in bold line, this isotherm represents the instantaneous dimensionless average temperature $< T >= 0$, which has been obtained by taking the average of the dimensionless temperatures of the fluid in the sphere (see Eq. (1)). According to the definition of both; the buoyancy term and the dimensionless temperature (see Eqs. (3) and (1), respectively), the instantaneous dimensionless average temperature $< T >= 0$ defines the boundary between the hot (buoyant) fluid and the cold (descending) fluid. Notice that in the boundary layer development stage, the isotherm lines are located adjacent to the cooled wall. And because the motion of the fluid is mainly confined in the boundary layer (the diffusion effect is dominant), the isotherm lines remain as concentric spheres. It is seen that at the end of the boundary layer development stage (at time $t_b = 0.03$), the hot fluid is confined within an imaginary spherical enclosure, and it is surrounded by a mass of cold fluid that is enclosed in an imaginary spherical gap. In order to compare the numerical simulations with the scaling analysis, concerning the boundary layer thickness, we have taken as the characteristic length scale of $\delta_{T,b}$, the location of the instantaneous average temperature $< T >= 0$ within the flow domain. Fig. 4 (top row right panel) shows that the average temperature $< T >= 0$ at $t_b = 0.03$ defines a sphere with radius $R_b \approx 0.75$, hence the boundary layer thickness is $\delta_{T,b} \approx 0.25$, which is of the same order of magnitude as the one calculated by the scaling analysis (see Tab. 1). The stratification (middle row) and cooling-down (bottom row) stages will be discussed in Secs. 5.2 and 5.3, respectively.

Fig. 5 shows the isotherm lines for the three stages when the initial Rayleigh number is $Ra = 1 \times 10^4$. The panels on the top row correspond to the boundary layer development stage at $t = 0.004$, $t = 0.008$ and $t = 0.01$. It can be seen that the location of the instantaneous average temperature $< T >= 0$ at $t_b = 0.01$ (top row right panel), resembles an imaginary sphere with radius $R_b \approx 0.8$, therefore the boundary layer thickness calculated by the numerical simulation is $\delta_{T,b} \approx 0.2$, which is

also of the same order of magnitude as the one calculated by the scaling analysis (see Tab. 1). Fig. 6 shows the isotherm lines for the three stages when the initial Rayleigh number is $Ra = 1.5 \times 10^5$. The panels on the top row correspond to the boundary layer development stage at $t = 0.001$, $t = 0.002$ and $t = 0.003$. It can be seen that the location of the average temperature $< T >= 0$ at $t_b = 0.003$ (top row right panel), resembles an imaginary sphere with radius $R_b \approx 0.91$, therefore the boundary layer thickness calculated by the numerical simulation is $\delta_{T,b} \approx 0.09$, which is also of the same order of magnitude as the one calculated by the scaling analysis (see Tab. 1).

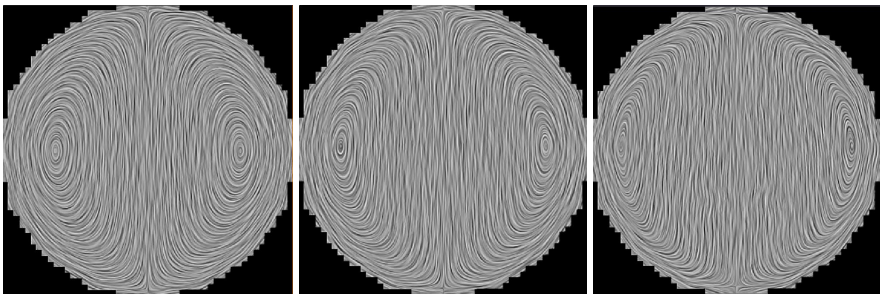

Figure 7: Stream lines at the end of the the boundary layer development stage. Left panel $Ra = 1 \times 10^3$ at $t_b = 0.03$, middle panel $Ra = 1 \times 10^4$ at $t_b = 0.01$ and right panel $Ra = 1.5 \times 10^5$ at $t_b = 0.003$.

5.2 Stratification stage

After the conduction-convection balance stage is attained, we have a spherical volume of hot fluid that is surrounded by a spherical gap of cold fluid (see Figs. 4-6). Fig. 7 shows (at the end of the boundary layer stage at t_b) the instantaneous streamlines for three initial Ra numbers: $Ra = 1 \times 10^3$, $Ra = 1 \times 10^4$ and $Ra = 1.5 \times 10^5$. It is clearly observed that the instantaneous stream lines in the sphere resemble a spherical vortex ring, which has been the subject of numerous studies [Griffiths and Campbell (1990), Lundgren and Mansour (1991), Lundgren, Yao, and Mansour (1992), Shusser and Gharib (2000), Rogers and Morris (2005)]. Shusser and Gharib (2000) (and references therein) pointed out that one way to produce a vortex ring is by releasing a lighter (or heavier) fluid into a different ambient fluid. In this case the energy required for the vortex ring formation is provided by the action of the buoyancy force. This ring is called a buoyant vortex ring. If the buoyancy is confined to a limited volume of fluid (as is the subject of this paper) the physical situation is known as a buoyant thermal. Shusser and Gharib (2000) putted forward

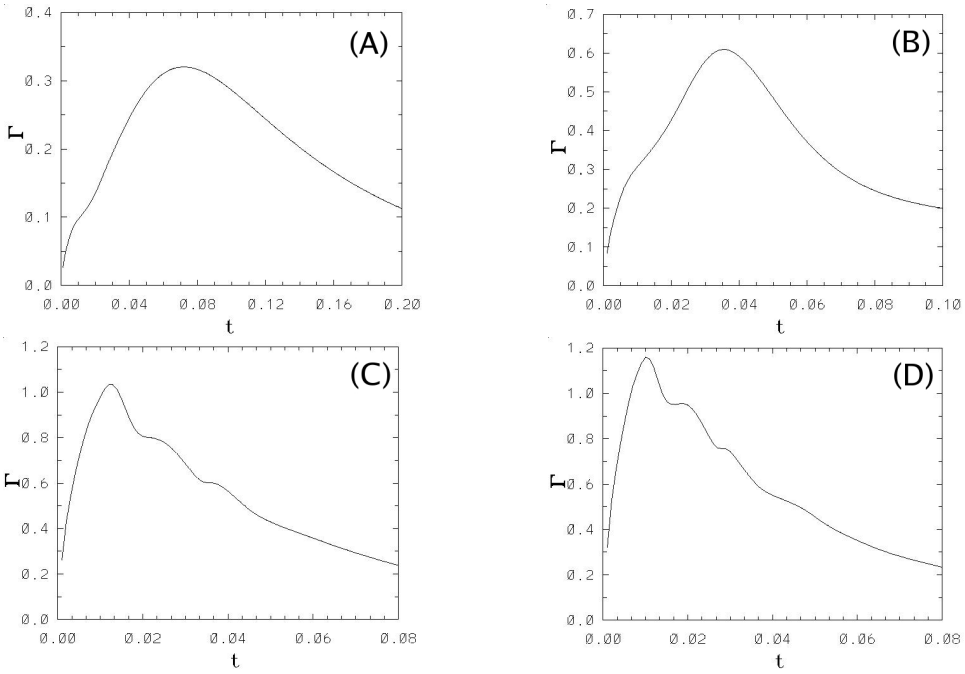

Figure 8: Dimensionless circulation Γ (within the meridional plane whose unit normal is $\mathbf{i}_1$) as a function of time. Initial Rayleigh number Ra: (A) $Ra = 1 \times 10^3$, (B) $Ra = 1 \times 10^4$, (C) $Ra = 1 \times 10^5$, (D) $Ra = 1.5 \times 10^5$.

the hypothesis that the process of buoyant vortex ring formation consists of two stages: (i) the continuous creation of the circulation and formation of the vortex ring (boundary layer development stage), and (ii) the growth of the vortex ring due to the accumulation of the generated circulation (stratification stage). By conducting experimental and numerical investigations of the vortex ring formation in buoyant thermals (downbursts), Lundgren, Yao, and Mansour (1992), estimated the characteristic time scale for buoyant vortex ring formation t_o. In their formulation of a simple mathematical model for an idealized microburst, they neglected diffusion between the heavier (the downburst) and the lighter surrounding fluid, therefore along the vortex ring formation process, a sharp density discontinuity across the separating interface was always present. By assuming the Boussinesq approximation they obtained the following dimensional vortex ring formation characteristic time scale

$$t_o = \left(\frac{R\rho}{g_3 \Delta\rho} \right)^{1/2} \tag{20}$$

where $\Delta\rho = \rho_o - \rho$, and ρ is the density of the fluid in the vortex ring. If we use the Boussinesq approximation $\Delta\rho \sim \rho\beta\Delta T$, and substituting this expression in Eq. (20), we have

$$t_o \sim \left(\frac{R\rho}{g_3 \rho\beta\Delta T} \right)^{1/2} \tag{21}$$

By using in Eq. (21) the definition of the *Ra* number given by Eq. (5) and by assuming a Prandtl number *Pr*=1, we obtain the expression

$$t_o \sim \frac{R^2}{\alpha} \frac{1}{Ra^{1/2}}, \tag{22}$$

which is of the same order of magnitude as Eq. (13), therefore $t_o \sim t_b$. Tab. 1 shows the comparison between the dimensionless vortex ring formation characteristic time scales t_b and t_o, it is observed that the agreement is satisfactory. Regarding the characteristic velocity of a buoyant vortex ring that moves within a surrounding fluid at rest, it is supposed that due to the action of the viscous shear stresses, the outer layer of the vortex will induce motion to the inner layers. Shusser and Gharib (2000) pointed out that the characteristic velocity of the buoyant ring must be defined as the velocity u acquired by the thermal after it has travelled one characteristic length (the diameter of the thermal). They defined the characteristic dimensional velocity u as

$$u = (4g_3 R\Delta\rho/\rho)^{1/2} \tag{23}$$

Again by using in Eq. (23), the Boussinesq approximation, the definition of the *Ra* number (see Eq. (5)) and assuming a Prandtl number *Pr*=1, we arrive at the following expression:

$$u = \frac{2\alpha}{R} Ra^{1/2} \tag{24}$$

which is also of the same order as Eq. (15). Notice that Eq. (24), includes the factor 2, because it takes into account that the characteristic length scale of the buoyant vortex ring is its diameter, hence we may write $u/2 \sim u_{\theta,b}$. Tab. 1 also shows the comparison between the characteristic dimensionless velocity of a buoyant vortex and the local dimensionless velocity scale $u_{\theta,b}$ obtained by the scaling analysis (remember that the variables introduced in Eq. (1) are used to obtain the dimensionless

parameters shown in Tab. 1). The difference in the values is mainly because the velocity scale proposed by Shusser and Gharib (2000) is an average value, whereas $u_{\theta,b}$ is a local velocity evaluated at the angle $\pi/2$ from the north pole. Therefore we may conclude that we have a successful agreement. Rosenfeld, Rambod, and Gharib (1998) carried out a numerical investigation to study the formation process, the evolution of the circulation, and the determination of the formation time scale (the formation number) of laminar axisymmetric vortex rings. They pointed out that the formation number is indicative of the time at which a vortex ring attains its maximum circulation. Fig. 8 shows the effect of the initial Rayleigh number *Ra* on the evolution of the circulation Γ of the vortex ring. The dimensionless circulation Γ shown in Fig. 8 was calculated as $\Gamma = \Gamma_m/(u_\theta R)$, where the dimensional u_θ has been evaluated at the end of the boundary layer stage, and at $\theta = \pi/2$, see Tab. 1, and Γ_m is the dimensional circulation which is calculated as

$$\Gamma_m = \int_S |\hat{\omega}_1| ds = |\overline{\hat{\omega}}_1| A_m, \tag{25}$$

where $|\overline{\hat{\omega}}_1|$ is the mean value of the magnitude of the dimensional vorticity component $\hat{\omega}_1$ within the plane whose unit normal is $\mathbf{i}_1$ (see Figs. 9 and 11 in which the dimensionless vorticity ω_1 is presented), and the dimensional surface of the plane is: $A_m = \pi R^2$.

Table 2: Maximum dimensionless circulation Γ_{max} and dimensionless time t_m at which the maximum value is attained see Fig. 8. Dimensionless time t_p at which initiates the first positive slope of the average Nusselt number $\overline{Nu}$ see Fig. 3.

Ra	Γ_{max}	t_m	t_p
10^3	0.32	0.072	0.07
10^4	0.61	0.035	0.025
10^5	1.03	0.012	0.01
1.5E10^5	1.16	0.01	0.008

Tab. 2 shows the maximum dimensionless circulation Γ_{max}, the dimensionless time t_m at which Γ_{max} is attained (the formation number) and the dimensionless time t_p at which initiates the first positive slope of the average Nusselt number $\overline{Nu}$, see Fig. 3. We may conclude that the time at which the maximum circulation is attained (the formation number), is closely related with the time at which the average Nusselt number $\overline{Nu}$ has the first positive slope (see Fig. 3). This is indicative of the intensity of motion within the sphere, which allows an increase of the heat transfer process.

In order to study the transient flow behaviour within the spherical container in the stratification stage, but in terms of the buoyant vortex ring theory, we take into ac-

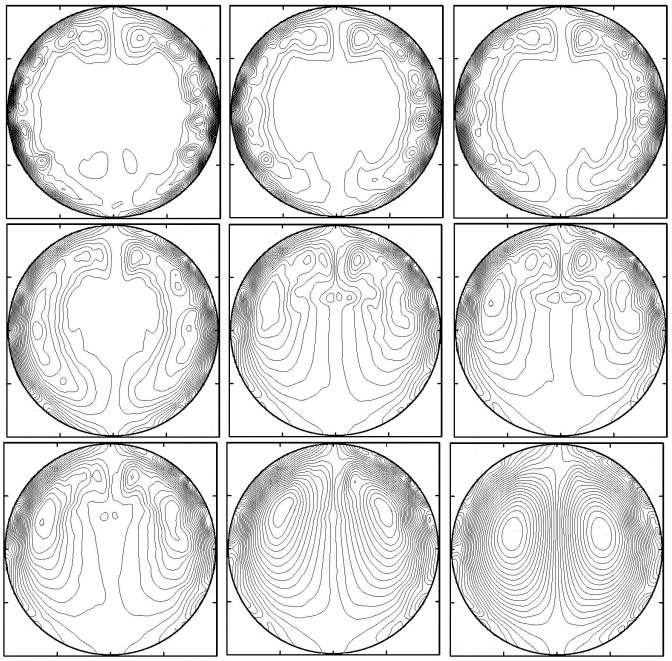

Figure 9: Numerical simulation of the dimensionless ω_1 vorticity contours. The the boundary layer development stage: Top row, from left to right: $t = 0.004$, [($x_2 = -0.96$, $x_3 = -0.19$, $\omega_1 = -269.4$), ($x_2 = 0.96$, $x_3 = -0.19$, $\omega_1 = 269.4$)]; $t = 0.008$, [($x_2 = -0.96$, $x_3 = 0.19$, $\omega_1 = -345.8$), ($x_2 = 0.96$, $x_3 = 0.19$, $\omega_1 = 345.8$)] and $t = 0.01$, [($x_2 = -0.96$, $x_3 = 0.19$, $\omega_1 = -369.9$), ($x_2 = 0.96$, $x_3 = 0.19$, $\omega_1 = 369.9$)]. The stratification stage: Middle row, from left to right: $t = 0.02$, [($x_2 = -0.96$, $x_3 = 0.19$, $\omega_1 = -442.0$), ($x_2 = 0.96$, $x_3 = 0.19$, $\omega_1 = 442.0$)]; $t = 0.04$, [($x_2 = -0.81$, $x_3 = 0.54$, $\omega_1 = -524.2$), ($x_2 = 0.81$, $x_3 = 0.54$, $\omega_1 = 524.2$)] and $t = 0.06$, [($x_2 = -0.81$, $x_3 = 0.54$, $\omega_1 = -369.2$), ($x_2 = 0.81$, $x_3 = 0.54$, $\omega_1 = 369.2$)]. The cooling-down stage: Bottom row, from left to right: $t = 0.1$, [($x_2 = -0.81$, $x_3 = 0.54$, $\omega_1 = -180.6$), ($x_2 = 0.81$, $x_3 = 0.54$, $\omega_1 = 180.6$)]; $t = 0.2$, [($x_2 = -0.81$, $x_3 = 0.54$, $\omega_1 = -54.3$), ($x_2 = 0.81$, $x_3 = 0.54$, $\omega_1 = 54.3$)] and $t = 0.4$, [($x_2 = -0.39$, $x_3 = 0.18$, $\omega_1 = -6.8$), ($x_2 = 0.39$, $x_3 = 0.18$, $\omega_1 = 6.8$)]. For initial Rayleigh number $Ra = 1 \times 10^4$.

count three concepts: (i) the spherical vortex ring bubble, which has been studied by Lundgren, Yao, and Mansour (1992), (ii) the formation of a vortex ring that is confined within the head of a buoyant laminar starting plume, which has been investigated by Rogers and Morris (2009), and (iii) the modification of the spatial distri-

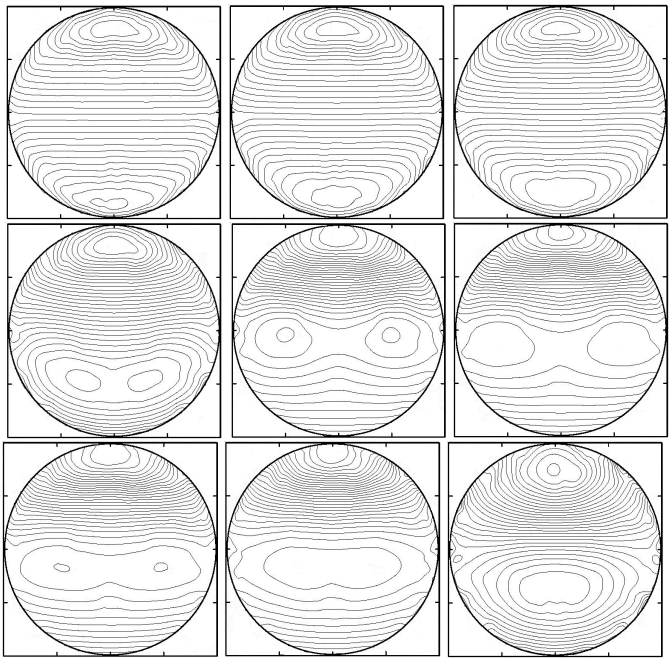

Figure 10: Numerical simulation of the dimensionless pressure contours. The boundary layer development stage: Top row, from left to right: $t = 0.004$, [($x_2 = 0.0$, $x_3 = -0.89$, $p = -1619.3$), ($x_2 = 0.0$, $x_3 = 0.89$, $p = 1664.4$)], $t = 0.008$, [($x_2 = \pm 0.05$, $x_3 = -0.88$, $p = -1631.8$), ($x_2 = 0.0$, $x_3 = 0.89$, $p = 1877.1$)] and $t = 0.01$, [($x_2 = \pm 0.05$, $x_3 = -0.88$, $p = -1513.7$), ($x_2 = 0.0$, $x_3 = 0.89$, $p = 1920.2$)]. The stratification stage: Middle row, from left to right: $t = 0.02$, [($x_2 = \pm 0.18$, $x_3 = -0.39$, $p = -968.1$), ($x_2 = 0.0$, $x_3 = 0.89$, $p = 2247.2$)], $t = 0.04$, [($x_2 = \pm 0.59$, $x_3 = -0.04$, $p = -1001.7$), ($x_2 = 0.0$, $x_3 = 0.89$, $p = 3753.1$)] and $t = 0.06$, [($x_2 = \pm 0.58$, $x_3 = -0.12$, $p = -641.1$), ($x_2 = 0.0$, $x_3 = 0.89$, $p = 2575.4$)]. The cooling-down stage: Bottom row, from left to right: $t = 0.1$, [($x_2 = \pm 0.39$, $x_3 = -0.18$, $p = -302.0$), ($x_2 = 0.0$, $x_3 = 0.89$, $p = 1166.1$)], $t = 0.2$, [($x_2 = \pm 0.3$, $x_3 = -0.15$, $p = -72.1$), ($x_2 = 0.0$, $x_3 = 0.89$, $p = 293.5$)] and $t = 0.4$, [($x_2 = 0.0$, $x_3 = -0.3$, $p = -8.2$), ($x_2 = 0.0$, $x_3 = 0.79$, $p = 14.3$)]. For initial Rayleigh number $Ra = 1 \times 10^4$.

bution of vorticity that allows the manipulation of the net volume of fluid entrained by the vortex ring, which has been investigated by Dabiri and Gharib (2004) and Dabiri (2006). Based on these concepts, firstly, we assume that the surface tension of the spherical bubble (our container) has an infinite value, therefore the bubble

will not be deformed by the interaction with the surrounding fluid (pressure difference) [Lundgren, Yao, and Mansour (1992)]. Secondly the fluid confined within our infinite surface tension bubble, has no mixing with the surrounding fluid, therefore the fluid within the bubble, behaves itself as an isolated vortex ring confined in a compact structure of spherical shape. And thirdly by modifying the vorticity distribution of the vortex ring via the variation of the initial Rayleigh number Ra, the diffusive mechanism of the ambient fluid entrainment may be altered [Dabiri and Gharib (2004); Dabiri (2006)]. It should be noted that the physical model of this investigation; a spherical vortex ring confined in a compact structure that does not allow the free growth of the vortex, can be considered as a limit case of the investigation carried out by Dabiri and Gharib (2004).

Figs. 4-6 and 7, show that at the end of the boundary layer development stage we have a vortex ring with the shape of a spherical hot bubble, surrounded by cold mass of the same fluid. Fig. 4 shows that in the stratification stage (middle row), the entrainment of cold fluid from the wall region, confines the hot fluid in the upper part of the sphere. Note that due to the small velocity of the upward flow in the core, the isotherm lines are not deformed (they remain as circles). Fig. 5 shows that in the stratification stage (middle row), the entrainment of cold fluid, confines the hot fluid in the upper part of the sphere. Due to the high velocity of the upward flow in the core, the isotherm lines become skewed. Note the increase of the temperature gradient (heat transfer rate) at the wall of the upper hemisphere, however in the lower hemisphere the heat transfer is reduced due to the stratification process. Fig. 6 shows that in the stratification stage (middle row), the entrainment of the cold fluid leads to an erratic and oscillatory motion of the fluid. In the left panel $t = 0.02$, the flow in the core is upwards, whereas in the central panel $t = 0.04$, the flow in the core is downwards, and in the right panel $t = 0.06$, the flow in the core again is upwards. Due to the high velocity of the entrained fluid, the isotherm lines are skewed. Note the high temperature gradient in the region surrounding the north pole, however the heat transfer rate in the lower hemisphere is reduced.

Maxworthy (1972) developed a simple mechanistic theory to model the entrainment of fluid into stable vortex rings. In his experimental investigation, he observed the following behaviour: (i) the surrounding fluid is entrained into the vortex during its formation, (ii) the vorticity in the vortex is not distributed linearly along the radial direction, (iii) the vorticity distribution has a distinctly smaller slope close to and at the symmetry axis than near the surface of the vortex ring, and (iv) the vorticity was not concentrated in a thin core. Figs. 9 and 11 show (for the cases with $Ra = 1 \times 10^4$ and $Ra = 1.5 \times 10^5$) the dimensionless vorticity field in the meridional

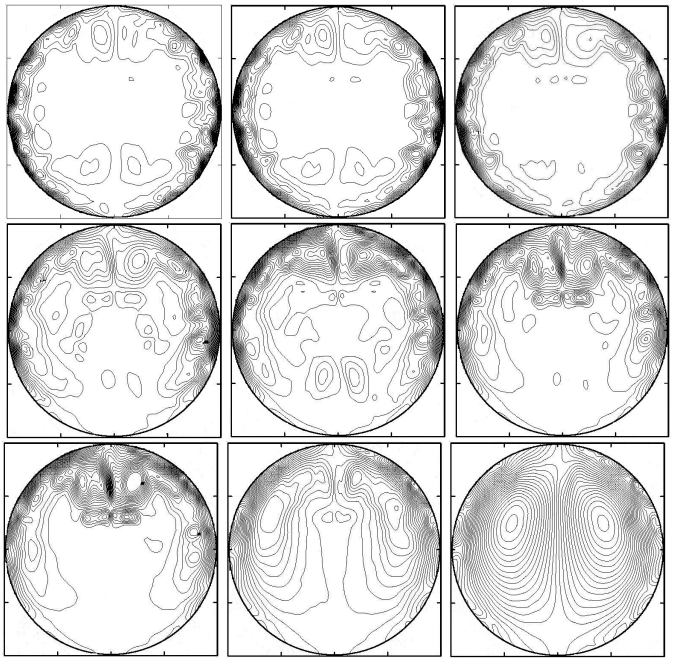

Figure 11: Numerical simulation of the dimensionless ω_1 vorticity contours. The boundary layer development stage: Top row, from left to right: $t = 0.001$, [($x_2 = -0.98$, $x_3 = 0.06$, $\omega_1 = -2408.6$), ($x_2 = 0.98$, $x_3 = 0.06$, $\omega_1 = 2408.6$)], $t = 0.002$, [($x_2 = -0.96$, $x_3 = -0.19$, $\omega_1 = -3158.8$), ($x_2 = 0.96$, $x_3 = -0.19$, $\omega_1 = 3158.8$)] and $t = 0.003$, [($x_2 = -0.96$, $x_3 = -0.19$, $\omega_1 = -3663.7$), ($x_2 = 0.96$, $x_3 = -0.19$, $\omega_1 = 3663.7$)]. The stratification stage: Middle row, from left to right: $t = 0.017$, [($x_2 = -0.98$, $x_3 = -0.06$, $\omega_1 = -4714.1$), ($x_2 = 0.98$, $x_3 = -0.06$, $\omega_1 = 4714.1$)], $t = 0.025$, [($x_2 = -0.74$, $x_3 = 0.65$, $\omega_1 = -3524.9$), ($x_2 = 0.74$, $x_3 = 0.65$, $\omega_1 = 3524.9$)] and $t = 0.038$, [($x_2 = -0.81$, $x_3 = 0.54$, $\omega_1 = -3040.9$), ($x_2 = 0.81$, $x_3 = 0.54$, $\omega_1 = 3040.9$)]. The cooling-down stage: Bottom row, from left to right: $t = 0.06$, [($x_2 = -0.74$, $x_3 = 0.65$, $\omega_1 = -1853.2$), ($x_2 = 0.74$, $x_3 = 0.65$, $\omega_1 = 1853.2$)], $t = 0.2$, [($x_2 = -0.81$, $x_3 = 0.54$, $\omega_1 = -168.7$), ($x_2 = 0.81$, $x_3 = 0.54$, $\omega_1 = 168.7$)] and $t = 0.4$, [($x_2 = -0.37$, $x_3 = 0.27$, $\omega_1 = -16.1$), ($x_2 = 0.37$, $x_3 = 0.27$, $\omega_1 = 16.1$)]. For initial Rayleigh number $Ra = 1.5 \times 10^5$.

plane whose unit normal vector is $\mathbf{i}_1$;

$$\omega_1 = \left(\frac{\partial v_3}{\partial x_2} - \frac{\partial v_2}{\partial x_3} \right). \tag{26}$$

In each panel of the figures, we have plotted twenty nine dimensionless iso-contours

of vorticity equally spaced between the minimum and the maximum values of the ω_1 field. The minimum and maximum values of ω_1 as well as the position where they take place, are written within the round brackets in the caption of each figure. Note that the ω_1 values on the right hand side of the meridional plane are positive (clockwise rotation), whereas on the left hand side they are negative (counterclockwise rotation). The panels on the top row of Fig. 9 show the ω_1 contours in the boundary layer development stage ($t = 0.004$, $t = 0.008$ and $t = 0.01$). It is seen that as time elapses: (i) the vorticity is increasing, (ii) the minimum and maximum values are distributed symmetrically with respect to the vertical axis, (iii) the position of the minimum and maximum values does not change ($x_2 = \pm 0.96$, $x_3 = -0.19$), remaining close to the wall of the enclosure, (iv) in the core of the sphere the vorticity is almost negligible, and (v) the vorticity gradient is higher close to the wall, particularly in the neighbourhood of the equator. The panels on the middle row of Fig. 9 show the ω_1 contours in the stratification stage ($t = 0.02$, $t = 0.04$ and $t = 0.06$). Note that as time elapses: (i) the vorticity reaches its maximum value, and after $t \sim 0.04$ the vorticity begins to decrease, (ii) the minimum and maximum values are distributed symmetrically with respect to the vertical axis, (iii) the position of the minimum and maximum values moves firstly upwards from $x_3 = -0.06$ to $x_3 = 0.65$ and secondly downwards from $x_3 = 0.65$ to $x_3 = 0.54$, but the radial position of the minimum and maximum values is adjacent to the wall $r \approx 0.98$, (iv) the vorticity gradient is higher close to the wall, and it is located in the upper hemisphere, (v) in the upper part of the core region the vorticity is accumulated, and (vi) in the lower part of the sphere the gradient of vorticity is small. Hence it is clearly observed than in the stratification stage the variation of vorticity is higher at the surface of the sphere than at the core, and the vorticity is not concentrated in a thin core [Maxworthy (1972)]. The panels on the bottom row of Fig. 9 show the ω_1 contours in the cooling-down stage ($t = 0.1$, $t = 0.2$ and $t = 0.4$), see Sec. 5.3. Note that as time elapses: (i) the vorticity is a decaying function of time, (ii) the minimum and maximum values are distributed symmetrically with respect to the vertical axis, (iii) the position of the minimum and maximum values moves from the upper region close to the wall ($x_2 = \pm 0.81$, $x_3 = 0.54$, $r = 0.97$), towards the upper core region ($x_2 = \pm 0.39$, $x_3 = 0.18$, $r = 0.42$), and (iv) the vorticity is evenly distributed in the sphere. A very similar description as the previous one can be given for the vorticity contours shown in Fig. 11. The panels on the top row show the ω_1 contours in the boundary layer development stage ($t = 0.001$, $t = 0.002$ and $t = 0.003$). Notice that as time elapses: (i) the vorticity is increasing, (ii) the minimum and maximum values are distributed symmetrically with respect to the vertical axis, (iii) the position of the minimum and maximum values moves downwards from ($x_2 = \pm 0.98$, $x_3 = 0.06$, $r = 0.98$) to ($x_2 = \pm 0.96$, $x_3 = -0.19$, $r = 0.97$), (iv) in the core the vorticity is almost negligible, and (v) the vorticity gra-

dient is higher close to the wall, in the region surrounding the equator. Panels on the middle row of Fig. 11 show the ω_1 contours in the stratification stage ($t = 0.017$, $t = 0.025$ and $t = 0.038$). Note that as time elapses: (i) the vorticity reaches its maximum value, and after $t \sim 0.017$ the vorticity decreases, (ii) the minimum and maximum values are distributed symmetrically with respect to the vertical axis, (iii) the position of the minimum and maximum values moves firstly upwards from $x_2 = \pm 0.98$, $x_3 = -0.06$, $r = 0.98$, to $x_2 = \pm 0.74$, $x_3 = 0.65$, $r = 0.98$ and secondly downwards from $x_2 = \pm 0.74$, $x_3 = 0.65$, $r = 0.98$ to $x_2 = \pm 0.81$, $x_3 = 0.54$, $r = 0.97$, points (iv)-(vi) of the previous description for the case with $Ra = 1 \times 10^4$, apply for the case $Ra = 1.5 \times 10^5$, currently under discussion. The panels on the bottom row of Fig. 11 show the ω_1 contours in the cooling-down stage ($t = 0.06$, $t = 0.2$ and $t = 0.4$), see Sec. 5.3. Note that as time elapses: (i) the vorticity is a decaying function of time, (ii) the minimum and maximum values are distributed symmetrically, (iii) the position of the minimum and maximum values moves from the upper wall region ($x_2 = \pm 0.74$, $x_3 = 0.65$, $r = 0.98$) towards the upper core region ($x_2 = \pm 0.37$, $x_3 = 0.27$, $r = 0.45$), and (iv) the vorticity is evenly distributed in the sphere.

Maxworthy (1972) qualitatively described the dynamical process of the entrainment of fluid into the vortex. He pointed out that as the vorticity diffuses from the interior of the vortex, the surrounding irrotational flow located in a thin layer pick ups the vorticity, dissipation occurs, then the total pressure in the layer is reduced and it is unable to traverse the vortex contour. Hence the surrounding fluid is entrained into the vortex ring, transporting the diffused vorticity with it. Fig. 10 shows the dimensionless pressure contours for the three stages of the transient process when $Ra = 1 \times 10^4$ (it should be mentioned that the pressure behaviour for the other three cases analyzed in this paper is very similar, then it will not be discussed here). In each panel of the figure, we have plotted twenty nine dimensionless iso-contours of pressure equally spaced between the minimum and the maximum values of the pressure field. The minimum and maximum values of the pressure as well as the position where they take place, are written within the round brackets in the caption of the figure. It is clearly shown that in the boundary layer development stage ($t = 0.004$, $t = 0.008$ and $t = 0.01$), the minimum (negative) value of the pressure at $t = 0.004$ is located in the lower part of the sphere along the vertical axis ($x_2 = 0.0$, $x_3 = -0.89$), whereas the maximum (positive) value is located at ($x_2 = 0.0$, $x_3 = 0.89$). As time elapses: (i) the change of the vertical position x_3 of the maximum and minimum values is small, (ii) at $t = 0.008$ and $t = 0.01$ there are two minimum (negative) pressures in the lower part of the sphere, which are distributed symmetrically with respect to the vertical axis, (iii) the maximum (positive) pressure in the upper part is increased, and (iv) the minimum (negative)

pressure in the lower part slightly oscillates. Panels on the middle row show the stratification stage ($t = 0.02$, $t = 0.04$ and $t = 0.06$). Note that as time elapses: (i) the minimum (negative) pressure in the lower part of the sphere slightly oscillates, (ii) the maximum (positive) pressure in the upper part reaches its maximum value, (iii) the vertical location of the minimum (negative) pressure moves up from $x_3 = -0.39$ to $x_3 = -0.04$ and then moves down to $x_3 = -0.12$, and (iv) there are two minimum (negative) pressures in the lower part of the sphere, which are distributed symmetrically with respect to the vertical axis, the minimum values move towards the wall. Panels on the bottom row show the cooling-down stage ($t = 0.1$, $t = 0.2$ and $t = 0.4$), see Sec. 5.3. Note that as time elapses: (i) the minimum (negative) pressure in the lower part diminishes its magnitude, (ii) the maximum (positive) pressure in the upper part also diminishes its magnitude, (iii) the vertical location of the minimum (negative) pressure moves down, (iv) the location of the maximum (positive) pressure also moves down, and (v) the two minimum (negative) pressures in the lower part of the sphere, which are distributed symmetrically with respect to the vertical axis, move towards the core. It is interesting to mention that in the stratification stage the minimum (negative) pressure region initially located close to the south pole, ascends towards the equator and occupies a large portion of the spherical cavity, specially from the equator to the south pole. It should be noted that in the stratification stage the pressure in the neighborhood of the south pole is higher than the pressure in the equatorial region, hence the fluid in the boundary layer is unable to traverse the vortex contour and entrainment sets in [Maxworthy (1972)]. At the onset of the entrainment, the stratification stage of the spherical container is initiated [Narain (1973)]. In order to develop scaling laws for the time that the stratification stage takes on, we assume that once the boundary layer is fully developed, the fluid in the sphere is stratified by the cooled fluid from the boundary layer. Following Lin and Armfield (2005) we assume that the dimensional time t_s for the full stratification of the whole fluid in the sphere will be at the moment when the volume of the fluid flowing within the descending boundary layer Q_{bl}, is equal to the volume of the sphere V_{sphere}. The rate of flow fluid through the boundary layer at $\pi/2$ is estimated as

$$Q_{bl} = u_\theta A_{bl} \tag{27}$$

where A_{bl} is the area through which pass the boundary layer flow, it is defined as

$$A_{bl} = \pi \left(2R\delta_{T,b} - \delta_{T,b}^2\right) \tag{28}$$

The dimensional time for the stratification of the fluid within the sphere t_s is ob-

tained as

$$t_s = \frac{V_{sphere}}{Q_{bl}} = \frac{4}{3}\frac{R^3}{u_\theta\left(2R\delta_{T,b} - \delta_{T,b}^2\right)} \tag{29}$$

The total elapsed time at the end of the stratification time is the summation $t_{bs} = t_b + t_s$. Tab. 3 shows the dimensionless time t_{bs} for different initial Rayleigh numbers Ra and the dimensionless time $t_{bs_{num}}$ obtained from the numerical simulation (see Fig. 3). We assume that the stratification stage ends when the average Nusselt number attains its maximum value. After this time we assume that the cooling down process sets in.

Table 3: Dimensionless scaling analysis results (at $\theta = \pi/2$) for the time at which ends the stratification stage $t_{bs} = t_b + t_s$. t_b see Eq. (13), t_s see Eq. (29). For dimensionless $t_{bs_{num}}$ values see Fig. 3.

Ra	Ra_θ	t_{bs}	$t_{bs_{num}}$
10^3	3875.7	0.136	0.14
10^4	38757.8	0.063	0.06
10^5	387578.4	0.031	0.046
1.5E10^5	581367.6	0.028	0.038

5.3 Cooling-down stage

During the whole process of the formation of the vortex ring, the fluid in the sphere is continuously cooled down due to the heat transfer through the wall of the container. The non-steady process finishes when the whole body of fluid has the same dimensional temperature as the temperature of the wall, $\overline{T}(t) = T_w$, or the dimensionless temperature at each point of the fluid is $T(t) = 0$, see Eq. (1). Taking into account that all the released heat to fully cool down the fluid in the sphere must pass through the spherical wall, the dimensional energy balance in the sphere can be written as [Mattor, Durgin, Bloznalis, and Schoenberg (1992); Lin and Armfield (2005)]

$$-\overline{h}A_{sphere}\left(\overline{T} - T_w\right) = \rho V_{sphere} C_p \frac{d\overline{T}}{dt}, \tag{30}$$

where $\overline{h}$ is the average heat transfer coefficient evaluated at the boundary of the sphere and A_{sphere} is the surface of the spherical wall. Carrying out the integration

and taking into account that the average heat transfer coefficient $\overline{h}$ is a function of time, the dimensional average temperature is written as;

$$\overline{T}(t) = T_w + \left(\overline{T}_i - T_w\right) \exp\left[-\frac{A_{sphere}}{\rho V_{sphere} C_p} \int_0^t \overline{h}(t) dt\right] \tag{31}$$

or

$$-T_{w^*} = \frac{\overline{T}(t) - T_w}{\overline{T}_i - T_w} = \exp\left[-\frac{A_{sphere}}{\rho V_{sphere} C_p} \int_0^t \overline{h}(t) dt\right], \tag{32}$$

where T_{w^*} is the dimensionless temperature at the wall of the sphere. The average heat transfer coefficient $\overline{h}(t)$ may be estimated from the average Nusselt number $\overline{Nu}(t)$ as

$$\overline{h}(t) = \frac{\overline{Nu}(t) k}{R}, \tag{33}$$

the $\overline{Nu}(t)$ number at the wall of the container is calculated as

$$\overline{Nu}(t) = \frac{1}{A_{sphere}} \int_{A_{sphere}} Nu \, dA = \frac{1}{A_{sphere}} \int_{A_{sphere}} \left[\frac{R}{k\left(\overline{T}(t) - T_w\right)} q_{rad}\bigg|_{r=R}\right] dA, \tag{34}$$

where q_{rad} is the heat flux evaluated at $r = R$, in the Cartesian coordinate system, it is calculated as

$$q_{rad}\bigg|_{r=R} = -k \nabla T \cdot \eta, \tag{35}$$

η is the outward unit vector normal to the surface of the sphere. The dimensionless expression of Eq. (34) is written as

$$\overline{Nu}(t) = \frac{1}{T_{w^*}} \frac{1}{A_{sphere}} \int_{A_{sphere}} \nabla T \cdot \eta \, dA. \tag{36}$$

Eq. (36) has been used to calculate the average Nusselt number $\overline{Nu}$ plotted in Fig. 3. In this investigation two procedures have been used to calculate the dimensionless temperature at the wall of the sphere T_{w^*}. In the first procedure we obtain an average value of T_{w^*}. This has been calculated by taking the mean value of the dimensionless temperature calculated at the Gauss-Lobatto-Legendre points (of the spectral element method) located on the surface of the sphere. In the second procedure we use the Lumped Capacity method represented by Eqs. (30)-(33). Fig.

12 shows the dimensionless temperature at the wall of the sphere $-T_{w^*}$ as a function of time for the four cases: $Ra = 1 \times 10^3$, $Ra = 1 \times 10^4$, $Ra = 1 \times 10^5$ and $Ra = 1.5 \times 10^5$. It can be seen that at small initial Ra number ($Ra = 1 \times 10^3$), the dimensionless temperature at the wall of the sphere $-T_{w^*}$ evaluated by taking the average of the Gauss-Lobatto-Legendre points, follows the analytical solution for the pure conductive regime $-T_{w^*}^{cond}(t)$ (plotted as a continuous line). It is seen that at $Ra = 1 \times 10^3$, the solution obtained by the Lumped Capacity method is higher than the averaging procedure. As the initial Ra number is increased, $-T_{w^*}$ decreases much faster than the conductive regime, hence the Lumped Capacity method and the averaging process are close each other. For $Ra \geq 1 \times 10^5$, the mixing by the entrainment leads to a decrease of the time for cooling down. The continuous line in the graphs of Fig. 12, represents the analytical solution of the dimensionless temperature at the wall $-T_{w^*}^{cond}(t)$ for the pure conductive case. In the conductive regime the temperature $-T_{w^*}^{cond}(t)$ as a function of time of the fluid confined in a spherical container with initial uniform dimensional temperature $\overline{T}_i$ and uniform dimensional wall temperature $T_w = 0$, is given as [Carslaw and Jaeger (1959)]:

$$-T_{w^*}^{cond}(t) = \frac{T_{av}^{cond}(t) - T_w}{\overline{T}_i - T_w} = \frac{6}{\pi^2} \sum_{n=1}^{\infty} \frac{1}{n^2} \exp\left[-\alpha n^2 \pi^2 t / R^2\right] \tag{37}$$

where $T_{av}^{cond}(t)$ is the dimensional average temperature of the fluid in the sphere. From Fig. 12 we conclude that the upper limit of the time to attain the full cooling down of the fluid in the sphere is provided by the pure conductive process. It is shown that by pure conduction, the required time is $t_c \sim 0.4$.

6 Unstable vortex rings

In the previous sections we have shown that at low initial Rayleigh numbers, $Ra \leq 1 \times 10^4$, the flow in the sphere behaves as two-dimensional and no oscillations appear, however as the initial Ra number is increased in the range $1 \times 10^5 \leq Ra \leq 1.5 \times 10^5$, the flow pattern shows an oscillatory, unstable behaviour. Chow and Akins (1975), in an experimental investigation, have reported that for Ra numbers greater that 1×10^7 (in a pseudosteady-state natural convection process), the flow is turbulent or perhaps transitional (unstable flow). They also found an oscillatory behaviour (up and down flow) with an erratic motion and irregular flow pattern. Fig. 13 shows, for the initial Rayleigh number $Ra = 1.5 \times 10^5$ case, the time evolution of the flow pattern in the time interval $0.016 \leq t \leq 0.049$, which corresponds mainly to the stratification stage, see Fig. 3. For this initial high Ra number case, the velocity of the descending cold fluid adjacent to the wall of the sphere, which also ascends in the core region, is capable to generate (in the region around the vertical

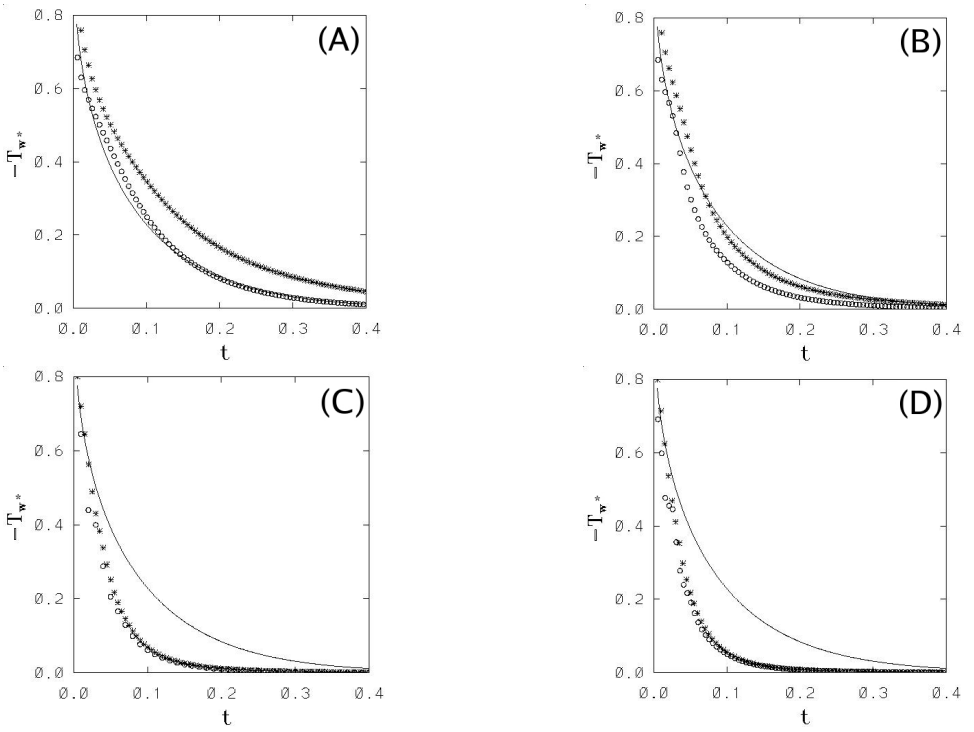

Figure 12: Dimensionless temperature at the wall of the sphere T_{w^*}. Initial Rayleigh number Ra: (A) $Ra = 1 \times 10^3$, (B) $Ra = 1 \times 10^4$, (C) $Ra = 1 \times 10^5$, (D) $Ra = 1.5 \times 10^5$. Circles: Averaging process of the Gauss-Lobatto-Legendre points. Asterisks: Lumped Capacity method, see Eq. (32). Continuous line: Analytical solution for the pure conductive case $T_{w^*}^{cond}$, see Eq. (37).

axis), a shear instability that leads to the formation of an internal vortex ring that spreads out as time elapses, simultaneously the center of the external vortex ring, slightly moves down, see the first and second rows from top to bottom. Notice that initially the center of the internal vortex ring that appears due to the shear instability (Kelvin-Helmholtz instability) is located in the upper part of the sphere, and at $t = 0.025$ (end of the second row from top to bottom) the center of the growing vortex has moved towards the equator. In the third row it is possible to observe how the size of the internal vortex ring diminishes, and the center of the external vortex moves up, towards the equator. At the end of the third row ($t = 0.03$), we observe that the internal vortex ring vanishes. In the fourth row, from top to bottom, we

observe that due to the internal thermal conditions, a new shear instability appears, conducting to the formation of an internal double vortex ring located in the upper part of the sphere. Simultaneously, the center of the external vortex ring slightly moves down, see panel at the end of the fourth row ($t = 0.039$). In the fifth row, it is possible to observe that the size of the new internal double vortex ring is increased and the center of the external vortex ring moves slightly down, see the panel at the end of the fifth row, $t = 0.044$. In the sixth row, it is shown how the internal double vortex ring again vanishes, whereas the center of the external vortex ring moves up, from the south hemisphere towards the equator region, see the panel at the end of the sixth row, $t = 0.049$. After this time, the cooling-down of the fluid does not allow the formation of an additional internal vortex ring.

Fig. 14 shows at $t = 0.018$ (at the beginning of the internal vortex ring formation), the stream lines for the $Ra = 1.5 \times 10^5$ case. We observe that along the vertical axis in the lower part, the flow is parallel (without vorticity, see Fig. 11, middle row at $t = 0.017$), whereas in the upper region, the internal three-dimensional vortex ring is forming.

7 Conclusions

Numerical simulations of the formation of a vortex ring that is confined in a spherical cavity, have been carried out by using the spectral element method. A scaling analysis has been used to develop the scaling laws for the relevant parameters characterizing the non-steady flow behaviour within the sphere. Three stages along the full cooling down process have been identified, and the the scaling laws developed for each stage, have been successfully compared with the results provided by the numerical method. At low Ra numbers the convective flow behaves as non-oscillatory and two-dimensional, hence the behaviour of the flow pattern is very similar to the results reported previously in the literature. However for high Ra numbers, we have found that the flow pattern shows an oscillatory, unstable behaviour. Numerical simulations of this irregular and oscillatory flow pattern, to the knowledge of the authors, have not been previously reported. In order to develop the scaling laws for the entrainment stage, we used the vortex ring formation theory, hence the circulation, vorticity and pressure fields were presented. We conclude that the amount of entrainment (and the rate of cooling) strongly depends on the pressure and vorticity fields. The results shown in this paper can be used in engineering applications, where the motion of the fluid within spherical containers, and its impact on the integrity of the spherical structure, should be taken into account to increase the performance of the containers.

Acknowledgement: Financial support for this investigation was provided by

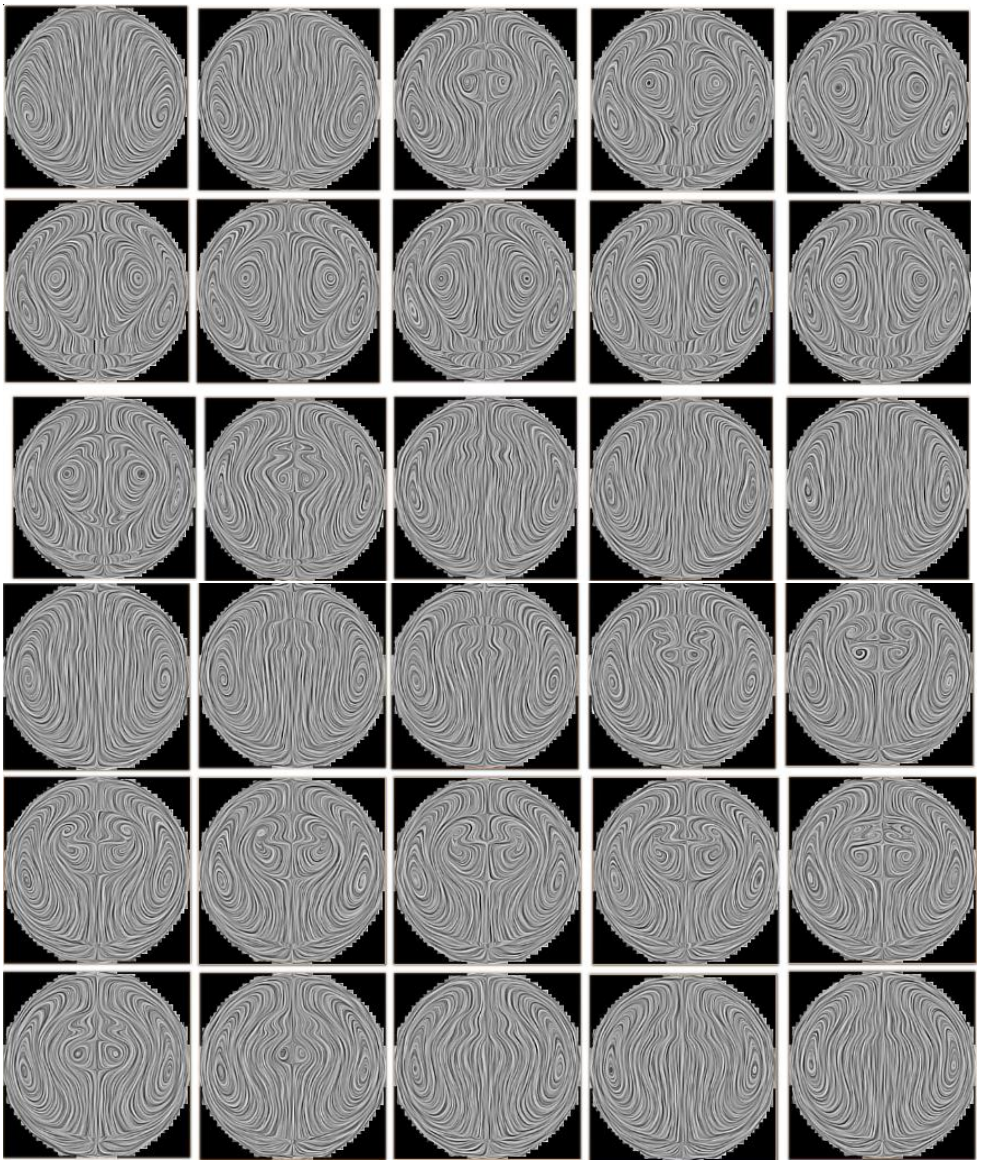

Figure 13: Unstable vortex ring. Time evolution of the convective patterns, for $Ra = 1.5 \times 10^5$. From top to bottom: first row: t=0.016, t=0.017, t=0.018, t=0.019, t=0.020. Second row: t=0.021, t=0.022, t=0.023, t=0.024, t=0.025. Third row: t=0.026, t=0.027, t=0.028, t=0.029, t=0.030. Fourth row: t=0.035, t=0.036, t=0.037, t=0.038, t=0.039. Fifth row: t=0.040, t=0.041, t=0.042, t=0.043, t=0.044. Sixth row: t=0.045, t=0.046, t=0.047, t=0.048, t=0.049.

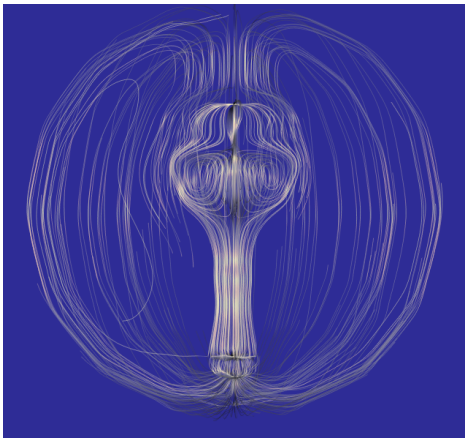

Figure 14: Unstable internal vortex ring formation at $t = 0.018$, for $Ra = 1.5 \times 10^5$.

DGAPA-UNAM (PAPIIT project IN102506-3) and DGSCA-UNAM through the Visualization Observatory (Ixtli project). Most of the computations were carried out in the supercomputers of DGSCA-UNAM.

References

Armfield, S.; Patterson, J. C.; Lin, W. (2007): Scaling investigation of the natural convection boundary layer on an evenly heated plate. *Int. Journal of Heat and Mass Transfer*, vol. 50, pp. 1592–1602.

Atluri, S. N.; Han, Z. D.; Rajendran, A. M. (2004): A new implementation of the meshless finite volume method, through the MLPG "Mixed approach". *CMES: Computer Modeling in Engineering & Sciences*, vol. 6, pp. 491–513.

Avila, R.; Pérez, A. (2008): A pressure correction approach coupled with the MLPG method for the solution of the Navier-Stokes equations. In M. Griebel and M. A. Schweitzer(Ed): *Lecture Notes in Computational Science and Engineering, Meshfree Methods for partial differential equations IV*, pp. 19–32. Springer.

Avila, R.; Solorio, F. J. (2009): Numerical solution of 2D natural convection in a concentric annulus with solid-liquid phase change. *CMES: Computer Modeling in Engineering & Sciences*, vol. 44, pp. 177–202.

Carslaw, H. S.; Jaeger, J. C. (1959): *Conduction of heat in solids*. Clarendon, Oxford.

Chow, M. Y.; Akins, R. G. (1975): Pseudosteady-state natural convection inside spheres. *Journal of Heat Transfer, Transactions of ASME*, vol. 97, pp. 54–59.

Dabiri, J. O. (2006): Note on the induced Lagrangian drift and added-mass of a vortex. *J. Fluid Mechanics*, vol. 547, pp. 105–113.

Dabiri, J. O.; Gharib, M. (2004): Fluid entrainment by isolated vortex rings. *J. Fluid Mechanics*, vol. 511, pp. 311–331.

Griffiths, R. W.; Campbell, I. H. (1990): Stirring and structure in mantle starting plumes. *Earth and Planetary Science Letters*, vol. 99, pp. 66–78.

Hutchins, J.; Marschall, E. (1989): Pseudosteady-state natural convection heat transfer inside spheres. *Int. J. of Heat and Mass tranfer*, vol. 32, pp. 2047–2053.

Karniadakis, G. E.; Sherwin, S. J. (1999): *Spectral/hp Element Methods for CFD*. Oxford University Press.

Lin, H.; Atluri, S. N. (2000): Meshless Local Petrov Galerkin (MLPG) method for convection-diffusion problems. *CMES: Computer Modeling in Engineering & Sciences*, vol. 1, pp. 45–60.

Lin, H.; Atluri, S. N. (2001): The Meshless Local Petrov-Galerkin (MLPG) method for solving incompressible Navier-Stokes equations. *CMES: Computer Modeling in Engineering & Sciences*, vol. 2, pp. 117–142.

Lin, W.; Armfield, S. (2005): Scaling laws for unsteady natural convection cooling of fluid with Prandtl number less than one in a vertical cylinder. *Physical Review E*, vol. 72, pp. 016306.

Lundgren, T. S.; Mansour, N. N. (1991): Vortex ring bubbles. *Journal of Fluid Mechanics*, vol. 224, pp. 177–196.

Lundgren, T. S.; Yao, J.; Mansour, N. N. (1992): Microburst modelling and scaling. *Journal of Fluid Mechanics*, vol. 239, pp. 461–488.

Mattor, E. E.; Durgin, W. W.; Bloznalis, P.; Schoenberg, R. (1992): *Analysis of natural convection in a low gravity environment*. AIAA PAPER 92-0603.

Maxworthy, T. (1972): The structure and stability of vortex rings. *J. Fluid Mechanics*, vol. 51, pp. 15–32.

Mitra, M.; Gopalakrishnan, S. (2006): Wavelet based 2-D spectral finite element formulation for wave propagation analysis in isotropic plates. *CMES: Computer Modeling in Engineering & Sciences*, vol. 15, pp. 49–67.

Narain, J. P. (1973): An isolated buoyant thermal in a stratified medium. *Atmospheric Environment*, vol. 7, pp. 979–989.

Parussini, L. (2007): Fictitious domain approach for spectral/hp element method. *CMES: Computer Modeling in Engineering & Sciences*, vol. 17, pp. 95–114.

Parussini, L.; Pediroda, V. (2007): Fictitious domain with Least-Squares spectral element method to explore geometric uncertainties by non-intrusive polynomial chaos method. *CMES: Computer Modeling in Engineering & Sciences*, vol. 22, pp. 41–63.

Patera, A. T. (1984): A spectral element method for fluid dynamics: laminar flow in a channel expansion. *Journal of Computational Physics*, vol. 54, pp. 468–488.

Patterson, J.; Imberger, J. (1980): Unsteady natural convection in a rectangular cavity. *J. Fluid Mechanics*, vol. 100, pp. 65–86.

Rogers, M. C.; Morris, S. W. (2005): Buoyant plumes and vortex rings in an autocatalytic chemical reaction. *Physical Review Letters*, vol. 95, pp. 024505.

Rønquist, E. M. (1988): *Optimal Spectral Element Methods for the unsteady three-dimensional incompressible Navier-Stokes equations*. Phd Thesis, Massachusetts Institute of Technology.

Rosenfeld, M.; Rambod, E.; Gharib, M. (1998): Circulation and formation number of laminar vortex rings. *J. Fluid Mechanics*, vol. 376, pp. 297–318.

Shusser, M.; Gharib, M. (2000): A model for vortex ring formation in a starting buoyant plume. *Journal of Fluid Mechanics*, vol. 416, pp. 173–185.

Whitley-III, H. G.; Vachon, R. I. (1972): Transient laminar free convection in closed spherical containers. *Journal of Heat Transfer, Transactions of ASME*, vol. 94, pp. 360–366.

Wu, C.-Y.; Al-Khoury, R.; Kasbergen, C.; Liu, X.-Y.; Scarpas, A. (2007): Spectral element approach for inverse models of 3D layered pavement. *CMES: Computer Modeling in Engineering & Sciences*, vol. 17, pp. 163–172.

Wu, C.-Y.; Liu, X.-Y.; Scarpas, A.; Ge, X.-R. (2006): Spectral element approach for forward models of 3D layered pavement. *CMES: Computer Modeling in Engineering & Sciences*, vol. 12, pp. 149–157.

Zhang, Y.; Khodadadi, J.; Shen, F. (1999): Pseudosteady-state natural convection inside spherical containers partially filled with a porous medium. *Int. J. of Heat and Mass tranfer*, vol. 42, pp. 2327–2336.